CMS Physics Analysis Summary

Contact: cms-pag-conveners-top@cern.ch 2017/09/18

Search for the standard model production of four top quarks with same-sign and multilepton final states in proton-proton collisions at $\sqrt{s} = 13$ TeV

The CMS Collaboration

Abstract

The standard model production of four top quarks ($\mathrm{t\bar{t}t\bar{t}}$) is studied by the CMS Collaboration using events containing at least three leptons (e, μ) or a same-sign pair. The events are produced in proton-proton collisions with a center-of-mass energy of 13 TeV at the LHC, and the data sample corresponds to an integrated luminosity of 35.9 fb^{-1}, recorded in 2016. Jet multiplicity and flavor are used to enhance signal sensitivity, and dedicated control regions are used to constrain the dominant standard model backgrounds. The observed (expected) significance is 1.6 (1.0) standard deviations, and the $\mathrm{t\bar{t}t\bar{t}}$ cross section is measured to be $16.9^{+13.8}_{-11.4}$ fb, in agreement with next-to-leading-order standard model predictions. These results are also used to constrain the Yukawa coupling of the top quark.

1 Introduction

The production of four top quarks ($t\bar{t}t\bar{t}$) is a rare standard model (SM) process, with representative leading order (LO) Feynman diagrams shown in Fig. 1. Many beyond-the-SM (BSM) theories predict an enhancement of the $t\bar{t}t\bar{t}$ cross section, such as gluino pair production in the supersymmetry framework [1–10], the pair production of scalar gluons [11, 12], and the production of a heavy pseudoscalar or scalar boson in association with a $t\bar{t}$ pair in Type II two-Higgs-doublet models (2HDM) [13–15]. Additionally, a top quark Yukawa coupling larger than expected in the SM can result in a significant increase of $t\bar{t}t\bar{t}$ production via an off-shell SM Higgs boson [16]. The SM cross section for $t\bar{t}t\bar{t}$ at $\sqrt{s} = 13$ TeV is predicted to be $9.2^{+2.9}_{-2.4}$ fb at next-to-leading order (NLO) [17]. Alternatively, the authors of Ref. [16] calculate a leading order cross section of $9.6^{+3.9}_{-3.5}$ fb at $\sqrt{s} = 13$ TeV, and then apply a NLO/LO K-factor of 1.27 based on the $\sqrt{s} = 14$ TeV evaluation of Ref. [18], resulting in a prediction of $12.2^{+5.0}_{-4.4}$ fb.

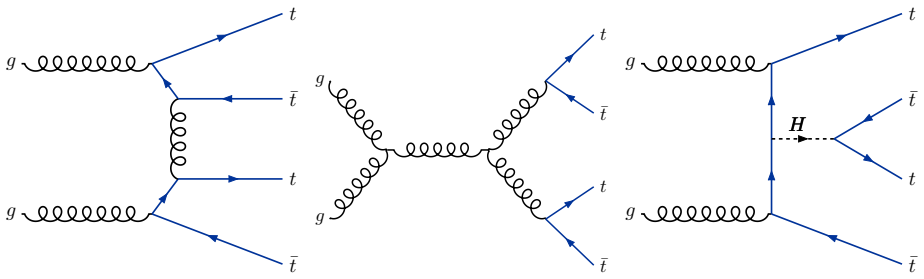

Figure 1: Representative Feynman diagrams for $t\bar{t}t\bar{t}$ production at LO in the SM.

After the decays of the top quarks the final state contains several jets resulting from the hadronization of light quarks and b quarks (b jets), and may contain isolated leptons and missing transverse momentum depending on the branching fractions of the W bosons [19]. Among these final states, the same-sign (SS) dilepton and the three (or more) lepton final states, considering electrons and muons and not including leptonic τ decays, correspond to branching fractions in $t\bar{t}t\bar{t}$ events of 8 and 1%, respectively. However, due to the low level of backgrounds, these channels are the most powerful ones to isolate $t\bar{t}t\bar{t}$ production with SM-like kinematics. The ATLAS and CMS Collaborations at the CERN LHC have previously searched for SM $t\bar{t}t\bar{t}$ production in both $\sqrt{s} = 8$ and 13 TeV pp collisions [20–23]. The most sensitive of these results is a by-product of the CMS SS dilepton search for BSM physics at $\sqrt{s} = 13$ TeV [23], with an observed (expected) $t\bar{t}t\bar{t}$ cross section upper limit of 42 (27^{+13}_{-8}) fb at 95% confidence level (CL).

The search of Ref. [23] is inclusive, exploring the final state with two SS leptons and at least two jets. The analysis described in this paper, which is based on the same data set corresponding to an integrated luminosity of 35.9 fb^{-1}, employs a signal categorization optimized for sensitivity for the SM $t\bar{t}t\bar{t}$ production, an improved b jet identification algorithm, and background estimation techniques that have been adapted to take into account the higher jet and b jet multiplicity requirements of the signal regions.

2 Background and signal simulation

Monte Carlo (MC) simulations at NLO are used to evaluate the $t\bar{t}t\bar{t}$ signal acceptance and to estimate the background from diboson (WZ, ZZ, Zγ, SS WW) and triboson (WWW, WWZ, WZZ, ZZZ, WWγ, WZγ) processes, as well as from processes with a single top quark (tWZ, tZq, tγ) or a $t\bar{t}$ pair produced in association with a boson ($t\bar{t}$W, $t\bar{t}$Z, $t\bar{t}$H). These samples are generated using the MADGRAPH5_AMC@NLO 2.2.2 [17] program with up to two additional partons in the matrix element calculation, except for the WZ, ZZ and $t\bar{t}$H samples, which are

generated with the POWHEG v2 [24, 25] program. The LO MADGRAPH5_AMC@NLO simulations, scaled to NLO cross sections [26], are used to estimate the Wγ and $\mathrm{t\bar{t}}\gamma$ processes with up to three additional partons. Other rare backgrounds, such as $\mathrm{t\bar{t}}$ production in association with dibosons ($\mathrm{t\bar{t}}$WW, $\mathrm{t\bar{t}}$WZ, $\mathrm{t\bar{t}}$ZZ, $\mathrm{t\bar{t}}$WH, $\mathrm{t\bar{t}}$ZW, $\mathrm{t\bar{t}}$HH) and triple top quark production ($\mathrm{t\bar{t}t}$, $\mathrm{t\bar{t}t}$W), are also generated using LO MADGRAPH5_AMC@NLO with no additional partons. The NNPDF3.0LO (NNPDF3.0NLO) [27] parton distribution functions (PDFs) are used to generate all LO (NLO) samples. Parton showering and hadronization, as well as SS WW from double-parton-scattering, are modeled by the PYTHIA 8.205 [28] program, while the MLM [29] and FxFx [30] prescriptions are employed when matching additional partons in the matrix element calculations to parton showers in the LO and NLO samples, respectively. Additional proton-proton interactions (pileup) within the same or nearby bunch crossings are also included in simulated events. The top quark mass in the generators is set to 172.5 GeV. The GEANT4 package [31] is used to model the response of the CMS detector.

To improve the MC modeling of the multiplicity of additional jets from initial-state radiation (ISR), simulated $\mathrm{t\bar{t}}$W and $\mathrm{t\bar{t}}$Z events are reweighted based on the number of ISR jets ($N_{\text{jets}}^{\text{ISR}}$). The reweighting is based on a comparison of the light-flavor jet multiplicity in dilepton $\mathrm{t\bar{t}}$ events in data and simulation. The method requires exactly two jets identified as originating from b quarks in the event, and assumes that all other jets are from ISR. To improve the modeling of the flavor of additional jets, the simulation is also corrected to account for the ratio of $\mathrm{t\bar{t}b\bar{b}}/\mathrm{t\bar{t}jj}$ cross sections measured by CMS in Ref. [32]. More details on these corrections and their uncertainties are provided in Section 6.

3 The CMS detector and event reconstruction

The central feature of the CMS detector is a superconducting solenoid of 6 m internal diameter, providing a magnetic field of 3.8 T. Within the solenoid volume are a silicon pixel and strip tracker, a lead tungstate crystal electromagnetic calorimeter (ECAL), and a brass and scintillator hadron calorimeter (HCAL), each composed of a barrel and two endcap sections. Forward calorimeters extend the pseudorapidity (η) coverage provided by the barrel and endcap detectors. Muons are measured in gas-ionization detectors embedded in the steel flux-return yoke outside the solenoid. A more detailed description of the CMS detector, together with a definition of the coordinate system used and the relevant kinematic variables, can be found in Ref. [33].

Events of interest are selected using a two-tiered trigger system [34]. The first level (L1), composed of custom hardware processors, uses information from the calorimeters and muon detectors to select events at a rate of around 100 kHz within a time interval of less than 4 μs. The second level, known as the high-level trigger (HLT), consists of a farm of processors running a version of the full event reconstruction software optimized for fast processing, and reduces the event rate to less than 1 kHz before data storage.

Events are processed using the particle-flow (PF) algorithm [35], which reconstructs and identifies each individual particle with an optimized combination of information from the various elements of the CMS detector. The energy of photons is directly obtained from the ECAL measurement. The energy of electrons is determined from a combination of the electron momentum at the primary interaction vertex as determined by the tracker, the energy of the corresponding ECAL cluster, and the energy sum of all bremsstrahlung photons spatially compatible with the electron track [36]. The momentum of muons is obtained from the curvature of the corresponding track, combining information from the silicon tracker and the muon system [37]. The

energy of charged hadrons is determined from a combination of their momentum measured in the tracker and the matching ECAL and HCAL energy deposits, corrected for the response function of the calorimeters to hadronic showers. The energy of neutral hadrons is obtained from the corresponding corrected ECAL and HCAL energies.

Hadronic jets are clustered from neutral PF candidates and charged PF candidates associated with the primary vertex, using the anti-k_T algorithm [38, 39] with a distance parameter $R = \sqrt{(\Delta\eta)^2 + (\Delta\phi)^2}$ of 0.4. The jet momentum is determined as the vectorial sum of all PF candidate momenta in the jet. An offset correction is applied to jet energies to take into account the contribution from pileup. Jet energy corrections are derived from simulation, and are improved with in situ measurements of the energy balance in dijet, multijet , γ+jet and leptonically decaying Z+jet events [40, 41]. Additional selection criteria are applied to each event to remove spurious jet-like features originating from isolated noise patterns in certain HCAL regions. Jets originating from b quarks are identified (b-tagged jets) using a deep neural network algorithm [42], with a working point chosen such that the efficiency to identify a b quark jet is in the range of 55–70% for jet p_T between 20 and 400 GeV. The misidentification rate for light-flavor jets is approximately 1%. The vector $\vec{p}_T^{\,miss}$ is defined as the projection on the plane perpendicular to the beams of the negative vector sum of the momenta of all reconstructed PF candidates in an event [43]. Its magnitude is referred to as p_T^{miss}. The scalar p_T sum of all jets in an event is referred to as H_T.

4 Event selection and search strategy

The definitions of the objects and the baseline event selection follow closely those of Refs. [23, 44]. Electron identification is based on a multivariate discriminant using shower shape and track quality variables. For muons the quality of the geometrical matching between tracker and muon system measurement is used. Isolation and impact parameter requirements are applied to both lepton flavors, as well as specific selections designed to improve the accuracy of the charge reconstruction, and to reject electrons originating from photon conversions. The combined reconstruction and identification efficiency is in the range of 45–70% (70–90%) for electrons (muons), increasing as a function of p_T and converging to the maximum value for $p_T > 60$ GeV. The number of leptons (N_{lep}), the number of jets (N_{jets}), and the number of b-tagged jets (N_b) are counted after the application of the basic kinematic requirements summarized in Table 1.

Table 1: Kinematic requirements for leptons and jets.

Object	p_T	$\lvert\eta\rvert$
Electrons	> 20 GeV	< 2.5
Muons	> 20 GeV	< 2.4
Jets	> 40 GeV	< 2.4
b-tagged jets	> 25 GeV	< 2.4

Signal events are selected using triggers that require two leptons with $p_T > 8$ GeV and $H_T > 300$ GeV. The trigger efficiency for events with at least one electron is $> 95\%$ and is around 92% for events with two muons. The initial baseline selection requires moderate H_T and p_T^{miss} ($H_T > 300$ GeV and $p_T^{miss} > 50$ GeV), at least two jets ($N_{jets} \geq 2$), two b-tagged jets ($N_b \geq 2$), a leading lepton with $p_T > 25$ GeV, and a second lepton of the same charge with $p_T > 20$ GeV. To reduce Drell–Yan backgrounds from charge-misidentified electrons, events with same-sign electron pairs forming an invariant mass below 12 GeV are rejected. Events where a third lepton with

p_T larger than 5 (7) GeV for muons (electrons) forms an opposite-sign (OS) same-flavor pair with mass below 12 GeV or between 76 and 106 GeV are also rejected. If the third lepton has $p_T > 20$ GeV and the invariant mass of the pair is between 76 and 106 GeV, these rejected events are used to populate a $t\bar{t}Z$ background control region (CRZ). After these requirements, 8 mutually exclusive signal regions (SRs) and a control region for the $t\bar{t}W$ background (CRW), are defined based on N_{jets}, N_b, and N_{lep}, as detailed in Table 2. The signal acceptance in the baseline region, including the leptonic W boson branching fraction, is approximately 1.5%.

Table 2: Definitions of the eight SRs and the two control regions for $t\bar{t}W$ (CRW) and $t\bar{t}Z$ (CRZ).

N_{lep}	N_b	N_{jets}	Region
2	2	≤ 5	CRW
		6	SR1
		7	SR2
		≥ 8	SR3
	3	5, 6	SR4
		≥ 7	SR5
	≥ 4	≥ 5	SR6
≥ 3	2	≥ 5	SR7
	≥ 3	≥ 4	SR8
Inverted Z veto			CRZ

5 Backgrounds

The main backgrounds to the $t\bar{t}t\bar{t}$ process in the SS dilepton and three (or more) lepton final states arise from rare multilepton processes, such as $t\bar{t}W$, $t\bar{t}Z$, and $t\bar{t}H$ ($H \to WW$), and single-lepton or OS dilepton processes with an additional "nonprompt lepton". Nonprompt leptons consist of hadrons misidentified as leptons, electrons from conversions of photons in jets, and leptons from the decays of heavy- or light-flavor hadrons. The minor background from OS dilepton events with a charge-misidentified lepton is also taken into account.

Rare multilepton processes are estimated using simulated samples. Control regions are used to constrain the normalization of the $t\bar{t}W$ and $t\bar{t}Z$ backgrounds, as described in Section 7, while for other processes the normalization is based on the NLO cross sections referenced in Section 2. Processes consisting of the associated production of a $t\bar{t}$ pair with a pair of bosons (including W, Z, and H) are grouped into a "$t\bar{t}VV$" category. Associated photon production processes such as $W\gamma$, $Z\gamma$, $t\bar{t}\gamma$, and $t\gamma$, where an electron is produced in an unidentified photon conversion, are grouped into a "$X\gamma$" category. All residual processes with very small contributions, including diboson (WZ, ZZ, SS WW from single- and double-parton scattering), triboson (WWW, WWZ, WZZ, ZZZ, $WW\gamma$, WZ γ), and rare single top quark (tZq, tWZ) and triple top quark processes ($t\bar{t}t$ and $t\bar{t}tW$), are grouped into a "Rare" category.

The nonprompt lepton and charge-misidentified lepton backgrounds are estimated following the methods described in Ref. [23]. For nonprompt leptons, an estimate referred to as the "tight-to-loose" method defines two control regions by modifying the lepton identification (including isolation) and event kinematic requirements, respectively. An "application region" is defined for every signal region by requiring that at least one of the leptons fails the standard identification ("tight") while satisfying a more relaxed one ("loose"). To obtain the nonprompt lepton background estimate in the corresponding signal region, the event yield in each application region is weighted by a factor of $\epsilon_{TL}/(1-\epsilon_{TL})$ for each lepton failing the tight requirement. The

ϵ_{TL} parameter is the probability that a nonprompt lepton satisfying a loose lepton selection also satisfies the tight selection. It is extracted as a function of lepton flavor and kinematics from a "measurement region" consisting of a single-lepton sample with event kinematic variables designed to suppress the $\mathrm{W} \to \ell\nu$ contribution.

For charge-misidentified leptons, an OS dilepton control region is defined for each SS dilepton signal region. Its yield is then weighted by the charge misidentification probability estimated in simulation, which ranges between 10^{-5} and 10^{-3} for electrons and is found to be negligible for muons.

6 Systematic uncertainties

Sources of experimental and theoretical uncertainties are considered for the data and simulated samples, as summarized in Table 3. The uncertainty in the integrated luminosity is 2.5% [45]. The simulation is reweighted to match the measured data distribution in the number of pileup collisions per event; the uncertainty in the inelastic cross section is propagated to the final yields with an effect at the level of 6% or less.

Trigger efficiencies are measured with an uncertainty of 2% from an independent data sample selected using single-lepton triggers. Lepton efficiency scale factors, accounting for differences in the reconstruction and identification efficiencies between data and simulation, are measured using a "tag-and-probe" method applied to a sample enriched in $\mathrm{Z} \to \ell\ell$ events [36, 37]. The scale factors are applied to all simulated processes with an uncertainty per lepton of approximately 3% for muons and 4% for electrons.

The uncertainty in the calibration of the jet energy scale (JES) depends on the transverse momentum and pseudorapidity of the jet and results in a 1–15% variation in the event yield in each signal region. The uncertainty due to the jet energy resolution is estimated by broadening the resolution in simulation [41], and the resulting effect is a change of 1–5% in the signal region yields. The b-tagging efficiency in simulation is corrected using scale factors determined from efficiencies measured in data and simulation [46]. The uncertainty in the measured scale factors results in an overall effect between 1 and 15%, depending on the signal region.

As described in Section 2, the simulation of $\mathrm{t\bar{t}W}$ and $\mathrm{t\bar{t}Z}$ events is reweighted to match the number of additional jets observed in data. The reweighting factors vary between 0.92 and 0.77 for $1 \leq N_j^{\mathrm{ISR}} \leq 4$. Half of the difference from unity is taken as a systematic uncertainty in these reweighting factors to cover variations observed when the factors are applied to reweight a single-lepton $\mathrm{t\bar{t}}$ sample. Simulated $\mathrm{t\bar{t}W}$ and $\mathrm{t\bar{t}Z}$ events with two b quarks not originating from a top quark are also weighted to account for the CMS measurement of $\sigma(\mathrm{t\bar{t}b\bar{b}})/\sigma(\mathrm{t\bar{t}jj})$, which was found to be a factor of 1.7 ± 0.6 larger than the Monte Carlo prediction [32]. In signal regions requiring four b-tagged jets, where the effect is dominant, this results in a systematic uncertainty of up to 15%.

Uncertainties in the renormalization and factorization scales and the PDFs affect the number of events expected (normalization) for simulated background processes, as well as the acceptance for the $\mathrm{t\bar{t}t\bar{t}}$ signal. The effects of these variations on the relative distribution of events among signal regions (shape) are also considered. For the $\mathrm{t\bar{t}W}$ and $\mathrm{t\bar{t}Z}$ backgrounds, the normalization uncertainty is 40%, while for $\mathrm{t\bar{t}H}$ a 50% normalization uncertainty reflects the signal strength of 1.5 measured by the CMS Collaboration [47]. For the Rare, $\mathrm{X}\gamma$, and $\mathrm{t\bar{t}VV}$ categories, normalization uncertainties are taken to be 50%. The shape uncertainty resulting from variations of the renormalization and factorization scales is as large as 15% for the $\mathrm{t\bar{t}W}$, $\mathrm{t\bar{t}Z}$, and $\mathrm{t\bar{t}H}$ back-

grounds, and 10% for the $\mathrm{t\bar{t}t\bar{t}}$ signal, while the effect of the PDFs is only 1%. For the signal, the uncertainty in the acceptance from variations of the scales (PDFs) is 2% (1%). Additionally, for the $\mathrm{t\bar{t}t\bar{t}}$ signal only, the scales that determine ISR and final-state radiation (FSR) emissions in the parton shower are also varied, resulting in a 6% change in the acceptance and shape variations as large as 15%.

For the nonprompt lepton and charge-misidentified lepton backgrounds, the statistical uncertainty from the application region varies depending on the signal region considered. The charge-misidentified electron background is assigned a systematic uncertainty of 20%, based on comparisons of the expected number of SS events estimated from an OS control sample and the observed SS yield in a control sample enriched in $\mathrm{Z} \to \mathrm{e^+e^-}$ events with one electron or positron having a misidentified charge.

In addition to the statistical uncertainty, the nonprompt lepton background is assigned an overall normalization uncertainty of 30% to cover variations observed in closure tests performed with simulated multijet and $\mathrm{t\bar{t}}$ samples. This uncertainty is increased to 60% for electrons with $p_\mathrm{T} > 50\,\mathrm{GeV}$, to account for trends observed at high p_T in the electron closure tests. In addition, we include an uncertainty related to the subtraction of events with prompt leptons (due to electroweak processes with a W or Z boson) in the measurement region. The overall effect of the electroweak background subtraction uncertainty on the nonprompt lepton background is between 1 and 50%, depending on the signal region considered. The prompt lepton contamination was also checked in the application region, where it was found to be below 1%.

Experimental uncertainties are treated as correlated among signal regions for all signal and background processes. Systematic uncertainties in the data-driven estimates and theoretical uncertainties are treated as uncorrelated between processes, but correlated amongst signal regions. Statistical uncertainties due to the limited size of the simulated samples and the number of events in data control regions are considered fully uncorrelated.

Table 3: Summary of the sources of uncertainty and their effect on the yields of different processes in the SRs. The first two groups list experimental and theoretical uncertainties, respectively, assigned to processes estimated using simulation. The third group lists uncertainties assigned to processes whose yield is estimated from data.

Source	Uncertainty (%)
Integrated luminosity	2.5
Pileup	0–6
Trigger efficiency	2
Lepton selection	4–10
Jet energy scale	1–15
Jet energy resolution	1–5
b tagging	1–15
Simulated sample size	1–10
Scale and PDF variations	10–15
ISR/FSR (signal only)	5–15
$\mathrm{t\bar{t}H}$ (normalization)	50
Rare, $\mathrm{X}\gamma$, $\mathrm{t\bar{t}VV}$ (norm.)	50
$\mathrm{t\bar{t}Z}$, $\mathrm{t\bar{t}W}$ (normalization)	40
Charge misidentification	20
Nonprompt leptons	30–60

7 Results and interpretation

The kinematic properties of events in the signal regions (SRs 1–8 as defined in Table 2) are shown in Fig. 2, where distributions of the main kinematic variables of the data (N_{jets}, N_{b}, H_{T}, and $p_{\text{T}}^{\text{miss}}$) are compared to the SM background predictions. The N_{jets} and N_{b} distributions for CRW and CRZ are shown in Fig. 3. In both of these figures we overlay the expected SM $\text{t}\bar{\text{t}}\text{t}\bar{\text{t}}$ signal, scaled by a factor of 5. The SM predictions are generally consistent with the observations, with some underestimates visible in CRW and CRZ.

The yields from SRs 1–8, CRW, and CRZ are combined in a maximum-likelihood fit, following the procedures described in Ref. [48] to obtain an estimate of the best-fit cross section for $\text{t}\bar{\text{t}}\text{t}\bar{\text{t}}$, the significance of the observation with respect to the background-only hypothesis, and the upper limit on the $\text{t}\bar{\text{t}}\text{t}\bar{\text{t}}$ cross section, The experimental and theoretical uncertainties described in Section 6 are incorporated in the likelihood as nuisance parameters and are profiled in the fit. The fitted values of the nuisance parameters are found to be consistent with their initial values within uncertainties. The nuisance parameters corresponding to the $\text{t}\bar{\text{t}}\text{W}$ and $\text{t}\bar{\text{t}}\text{Z}$ normalizations are scaled by 1.2 ± 0.3 and 1.3 ± 0.3, respectively, while other background contributions including $\text{t}\bar{\text{t}}\text{H}$ are scaled up by 1.1 or less. The signal and control region results after the maximum-likelihood fit (post-fit) are shown in Fig. 4, with the fitted $\text{t}\bar{\text{t}}\text{t}\bar{\text{t}}$ signal contribution added to the background predictions, and are given in Table 4. The $\text{t}\bar{\text{t}}\text{t}\bar{\text{t}}$ cross section is measured to be $16.9^{+13.8}_{-11.4}$ fb. The observed (expected) significance with respect to the background-only hypothesis is found to be 1.6 (1.0) standard deviations, where the expectation is based on the central value of the NLO SM cross section calculation of $9.2^{+2.9}_{-2.4}$ fb [17]. The observed 95% CL upper limit on the cross section, based on an asymptotic formulation [49] of the modified frequentist CL_{s} criterion [50, 51], is found to be 41.7 fb. The corresponding expected upper limit, assuming no SM $\text{t}\bar{\text{t}}\text{t}\bar{\text{t}}$ contribution to the data set, is $20.8^{+11.2}_{-6.9}$ fb, showing a significant improvement with respect to Ref. [23].

The $\text{pp} \to \text{t}\bar{\text{t}}\text{t}\bar{\text{t}}$ process has contributions from diagrams with virtual Higgs bosons, as shown in Fig. 1. The limits and measurements of the $\text{t}\bar{\text{t}}\text{t}\bar{\text{t}}$ cross section can then be used to constrain the Yukawa coupling, y_{t}, between the top quark and the Higgs boson. We constrain y_{t} assuming that the signal acceptance is not affected by the virtual Higgs boson diagrams. In Fig. 5 we show the measurement of the $\text{t}\bar{\text{t}}\text{t}\bar{\text{t}}$ cross section and its upper limit, as well as its SM prediction as a function of the absolute value of the ratio of the top quark Yukawa coupling to its SM value ($|y_{\text{t}}/y_{\text{t}}^{\text{SM}}|$), where $y_{\text{t}}^{\text{SM}} = m_{\text{t}}(\sqrt{2}G_{\text{F}})^{1/2} \approx 1$. The combined ATLAS and CMS measurement of the top quark Yukawa coupling [52], including all production and decay modes explored with the Run 1 dataset ($\sqrt{s} = 7$ and 8 TeV), is also displayed. The prediction for the $\text{t}\bar{\text{t}}\text{t}\bar{\text{t}}$ cross section as a function of y_{t}, including the theoretical uncertainty associated with varying the renormalization and factorization scales by a factor of 2, is derived from the LO calculation of Ref. [16], with an NLO/LO K-factor [18]. The central (upper, lower) value of the theoretical cross section band results in a 95% CL limit $|y_{\text{t}}/y_{\text{t}}^{\text{SM}}| < 2.27$ (2.03, 2.56).

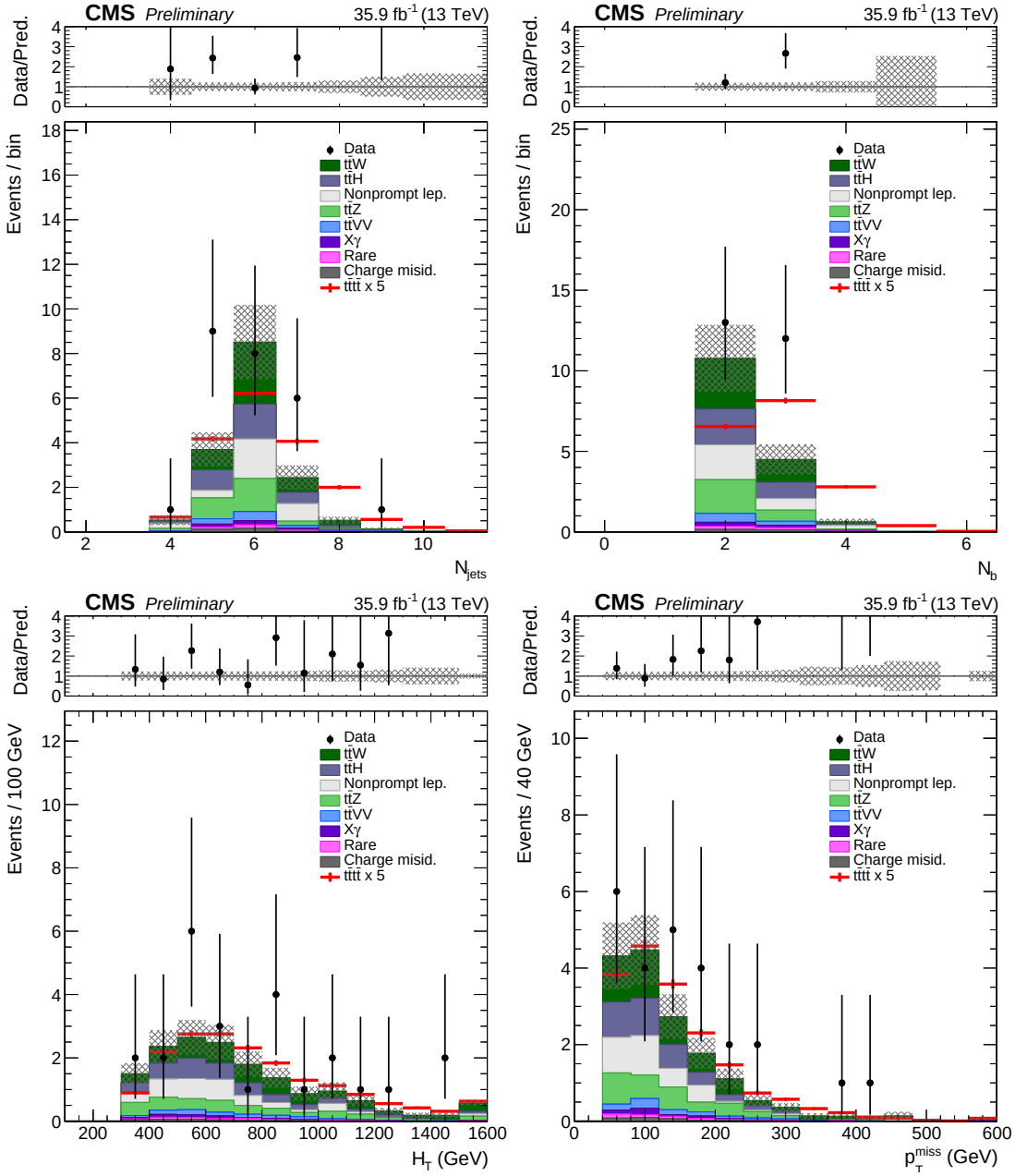

Figure 2: Distributions of the main analysis variables in the signal regions (SRs 1–8), before the fit to data: N_{jets}, N_{b}, H_{T}, and $p_{\text{T}}^{\text{miss}}$, where the last bin includes the overflow. The hatched area represents the total uncertainty in the SM background prediction, while the solid line represents the $\text{t}\bar{\text{t}}\text{t}\bar{\text{t}}$ signal, scaled by a factor of 5, assuming the SM cross section calculation from Ref. [17]. The upper panels show the ratio of the observed event yield and the total background prediction.

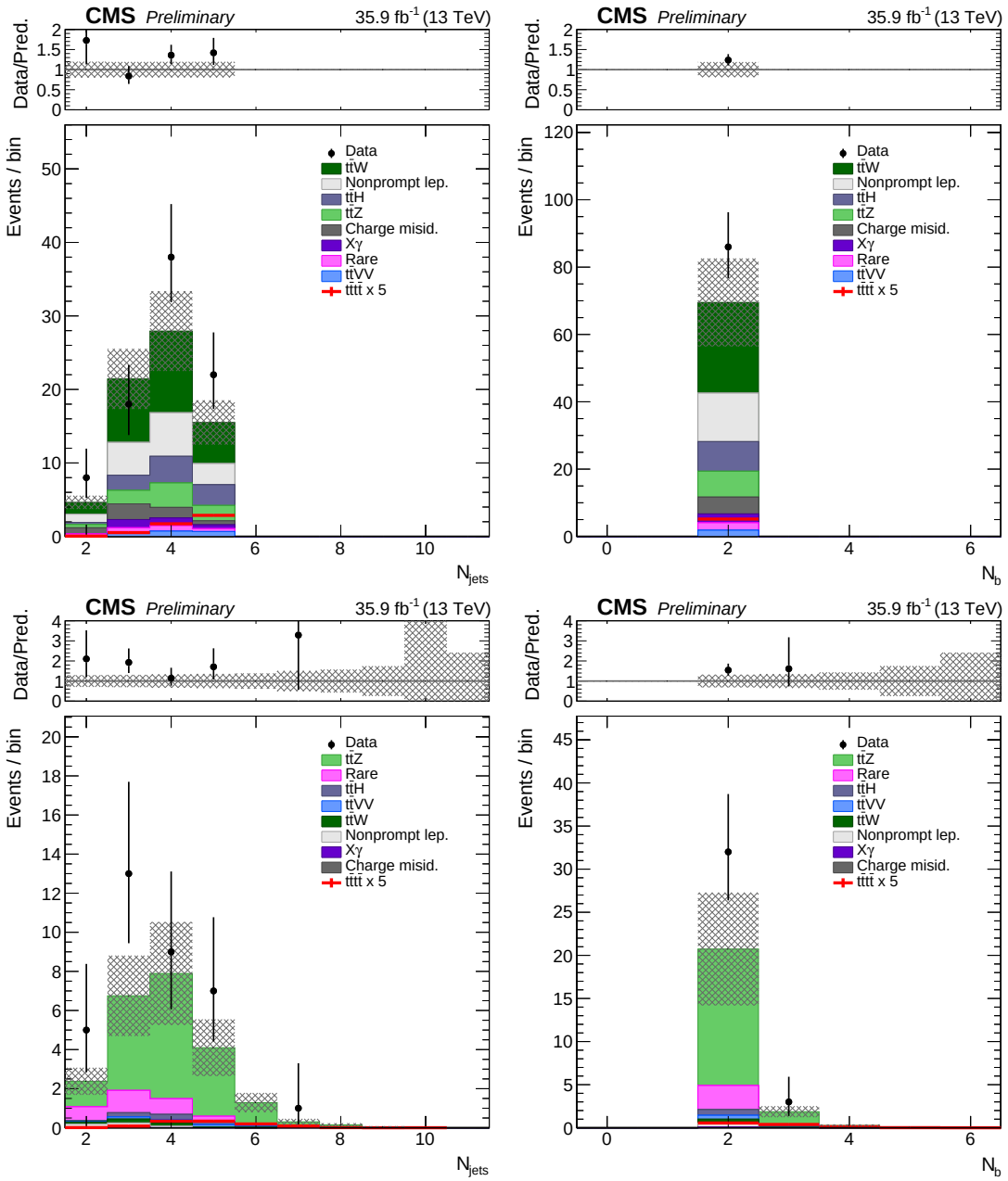

Figure 3: The N_{jets} (left) and N_{b} (right) distributions in the $\text{t}\bar{\text{t}}\text{W}$ (top) and $\text{t}\bar{\text{t}}\text{Z}$ (bottom) control regions, before the fit to data. The hatched area represents the total uncertainty in the SM background prediction, while the solid line represents the $\text{t}\bar{\text{t}}\text{t}\bar{\text{t}}$ signal, scaled by a factor of 5, assuming the SM cross section calculation from Ref. [17]. The upper panels show the ratio of the observed event yield and the total background prediction.

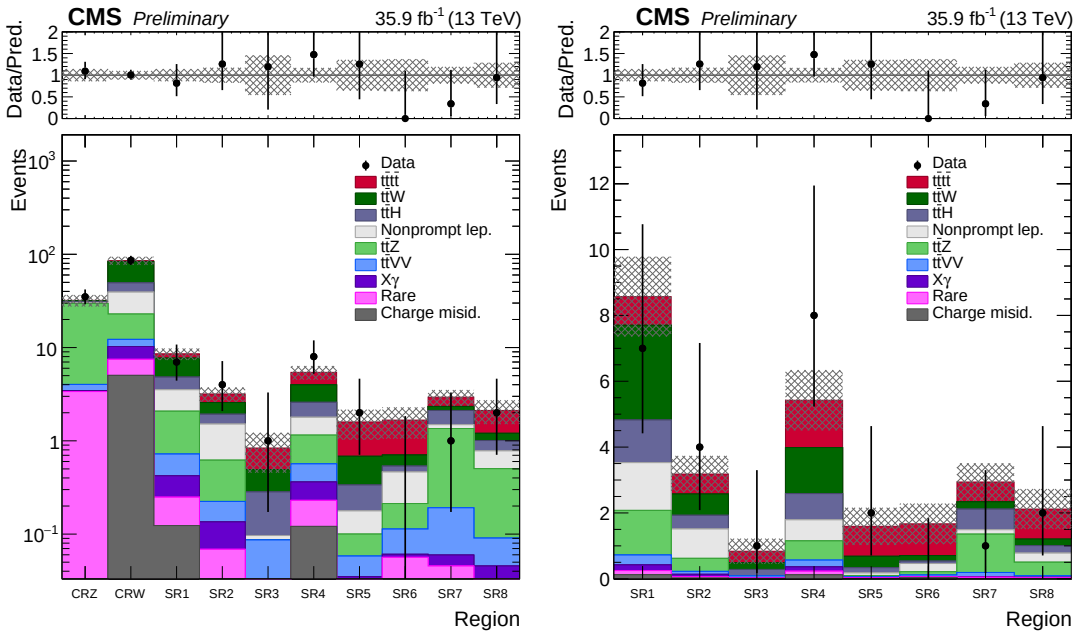

Figure 4: Observed yields in the analysis control and signal regions (left, in log scale), and signal regions only (right, in linear scale), compared to the post-fit predictions for signal and background processes. The hatched area represents the total uncertainty in the signal and background predictions. The upper panels show the ratio of the observed event yield and the total prediction of signal and background.

Table 4: The post-fit predicted background, signal, and total yields with their uncertainties and the observed number of events in the control and signal regions.

	SM background	$t\bar{t}t\bar{t}$	Total	Observed
CRZ	31.7± 4.6	0.4± 0.3	32.1± 4.6	35
CRW	83.7± 8.8	1.9± 1.2	85.6± 8.6	86
SR1	7.7± 1.2	0.9± 0.6	8.6± 1.2	7
SR2	2.6± 0.5	0.6± 0.4	3.2± 0.6	4
SR3	0.5± 0.3	0.4± 0.2	0.8± 0.4	1
SR4	4.0± 0.7	1.4± 0.9	5.4± 0.9	8
SR5	0.7± 0.2	0.9± 0.6	1.6± 0.6	2
SR6	0.7± 0.2	1.0± 0.6	1.7± 0.6	0
SR7	2.3± 0.5	0.6± 0.4	2.9± 0.6	1
SR8	1.2± 0.3	0.9± 0.6	2.1± 0.6	2

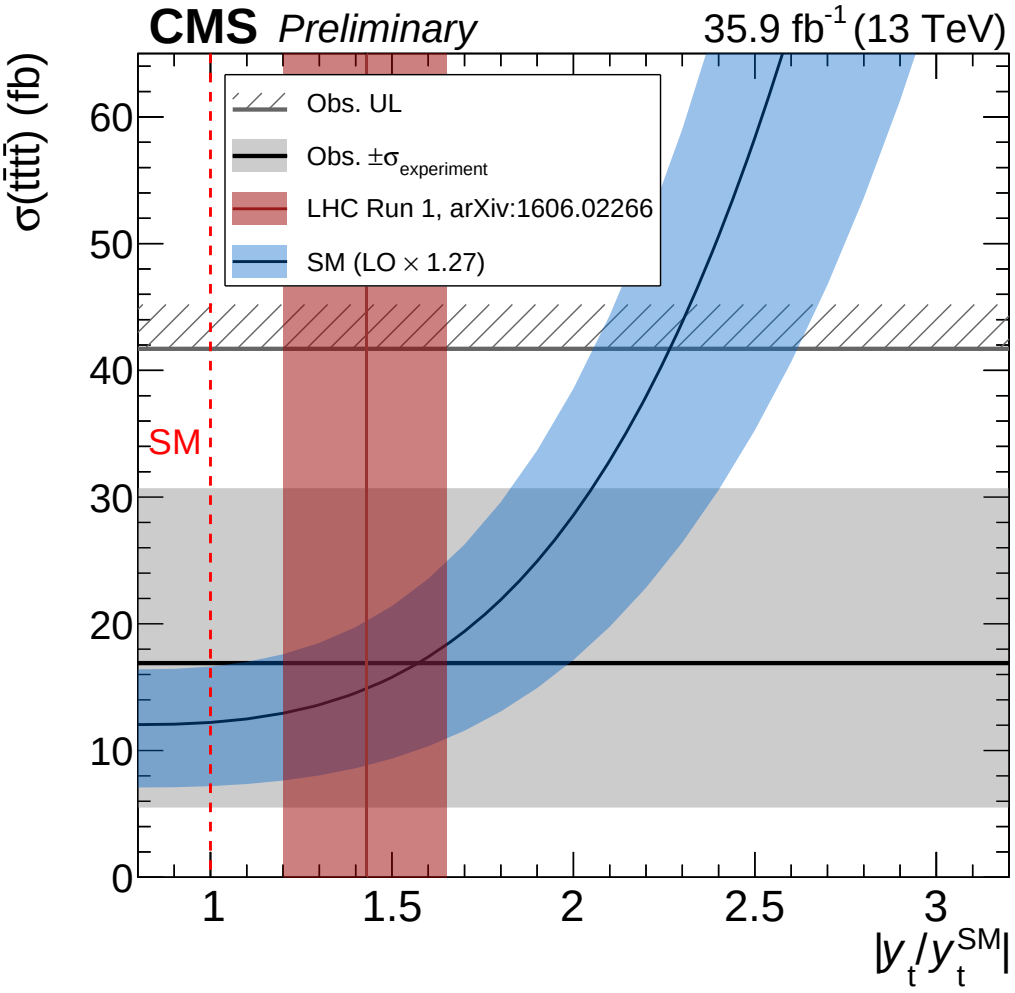

Figure 5: The expected $t\bar{t}t\bar{t}$ cross section, $\sigma(t\bar{t}t\bar{t})$, as a function of $|y_t/y_t^{SM}|$, the absolute value of the ratio of the top quark Yukawa coupling and its SM value (curved band), compared with the measured $\sigma(t\bar{t}t\bar{t})$ (horizontal band), and its 95% CL upper limit (horizontal line). See text for details.

8 Summary

We have presented the results of a search for the standard model $\mathrm{t\bar{t}t\bar{t}}$ process at the LHC, using data from $\sqrt{s} = 13\,\text{TeV}$ proton-proton collisions corresponding to an integrated luminosity of 35.9 fb^{-1}, collected with the CMS detector in 2016. The analysis strategy uses same-sign dilepton as well as three (or more) lepton events, relying on jet multiplicity and jet flavor to define search regions that are used to probe the $\mathrm{t\bar{t}t\bar{t}}$ process. Combining these regions yields a significance of 1.6 standard deviations with respect to the background-only hypothesis, and a measured $\mathrm{t\bar{t}t\bar{t}}$ cross section of $16.9^{+13.8}_{-11.4}$ fb, in agreement with the standard model predictions. The results are also interpreted to constrain the ratio of the top quark Yukawa coupling to its SM value, $|y_\mathrm{t}/y_\mathrm{t}^\mathrm{SM}| < 2.27$ at 95% confidence level.

References

[1] P. Ramond, "Dual theory for free fermions", *Phys. Rev. D* **3** (1971) 2415, doi:10.1103/PhysRevD.3.2415.

[2] Y. A. Gol'fand and E. P. Likhtman, "Extension of the algebra of Poincaré group generators and violation of P invariance", *JETP Lett.* **13** (1971) 323.

[3] A. Neveu and J. H. Schwarz, "Factorizable dual model of pions", *Nucl. Phys. B* **31** (1971) 86, doi:10.1016/0550-3213(71)90448-2.

[4] D. V. Volkov and V. P. Akulov, "Possible universal neutrino interaction", *JETP Lett.* **16** (1972) 438.

[5] J. Wess and B. Zumino, "A lagrangian model invariant under supergauge transformations", *Phys. Lett. B* **49** (1974) 52, doi:10.1016/0370-2693(74)90578-4.

[6] J. Wess and B. Zumino, "Supergauge transformations in four-dimensions", *Nucl. Phys. B* **70** (1974) 39, doi:10.1016/0550-3213(74)90355-1.

[7] P. Fayet, "Supergauge invariant extension of the Higgs mechanism and a model for the electron and its neutrino", *Nucl. Phys. B* **90** (1975) 104, doi:10.1016/0550-3213(75)90636-7.

[8] H. P. Nilles, "Supersymmetry, supergravity and particle physics", *Phys. Rept.* **110** (1984) 1, doi:10.1016/0370-1573(84)90008-5.

[9] S. P. Martin, "A supersymmetry primer", in *Perspectives on Supersymmetry II*, G. L. Kane, ed., p. 1. World Scientific, 2010. Adv. Ser. Direct. High Energy Phys., vol. 21. doi:10.1142/9789814307505_0001.

[10] G. R. Farrar and P. Fayet, "Phenomenology of the production, decay, and detection of new hadronic states associated with supersymmetry", *Phys. Lett. B* **76** (1978) 575, doi:10.1016/0370-2693(78)90858-4.

[11] T. Plehn and T. M. P. Tait, "Seeking Sgluons", *J. Phys. G* **36** (2009) 075001, doi:10.1088/0954-3899/36/7/075001, arXiv:0810.3919.

[12] S. Calvet, B. Fuks, P. Gris, and L. Valery, "Searching for sgluons in multitop events at a center-of-mass energy of 8 TeV", *JHEP* **04** (2013) 043, doi:10.1007/JHEP04(2013)043, arXiv:1212.3360.

[13] D. Dicus, A. Stange, and S. Willenbrock, "Higgs decay to top quarks at hadron colliders", *Phys. Lett. B* **333** (1994) 126, doi:10.1016/0370-2693(94)91017-0, arXiv:hep-ph/9404359.

[14] N. Craig et al., "The hunt for the rest of the Higgs bosons", *JHEP* **06** (2015) 137, doi:10.1007/JHEP06(2015)137, arXiv:1504.04630.

[15] N. Craig et al., "Heavy Higgs bosons at low tan β: from the LHC to 100 TeV", *JHEP* **01** (2017) 018, doi:10.1007/JHEP01(2017)018, arXiv:1605.08744.

[16] Q.-H. Cao, S.-L. Chen, and Y. Liu, "Probing Higgs width and top quark Yukawa coupling from $t\bar{t}H$ and $t\bar{t}t\bar{t}$ productions", *Phys. Rev. D* **95** (2017) 053004, doi:10.1103/PhysRevD.95.053004, arXiv:1602.01934.

[17] J. Alwall et al., "The automated computation of tree-level and next-to-leading order differential cross sections, and their matching to parton shower simulations", *JHEP* **07** (2014) 079, doi:10.1007/JHEP07(2014)079, arXiv:1405.0301.

[18] G. Bevilacqua and M. Worek, "Constraining BSM physics at the LHC: Four top final states with NLO accuracy in perturbative QCD", *JHEP* **07** (2012) 111, doi:10.1007/JHEP07(2012)111, arXiv:1206.3064.

[19] Particle Data Group, "Review of particle physics", *Chin. Phys. C* **40** (2016) 100001, doi:10.1088/1674-1137/40/10/100001.

[20] CMS Collaboration, "Search for standard model production of four top quarks in the lepton+jets channel in pp collisions at $\sqrt{s}$ = 8 TeV", *JHEP* **11** (2014) 154, doi:10.1007/JHEP11(2014)154, arXiv:1409.7339.

[21] ATLAS Collaboration, "Search for production of vector-like quark pairs and of four top quarks in the lepton-plus-jets final state in pp collisions at $\sqrt{s} = 8$ TeV with the ATLAS detector", *JHEP* **08** (2015) 105, doi:10.1007/JHEP08(2015)105, arXiv:1505.04306.

[22] CMS Collaboration, "Search for standard model production of four top quarks in proton-proton collisions at $\sqrt{s}$ = 13 TeV", *Phys. Lett. B* **772** (2017) 336, doi:10.1016/j.physletb.2017.06.064, arXiv:1702.06164.

[23] CMS Collaboration, "Search for physics beyond the standard model in events with two leptons of same sign, missing transverse momentum, and jets in proton-proton collisions at $\sqrt{s} = 13$ TeV", *Eur. Phys. J. C* **77** (2017) 578, doi:10.1140/epjc/s10052-017-5079-z, arXiv:1704.07323.

[24] T. Melia, P. Nason, R. Röntsch, and G. Zanderighi, "W^+W^-, WZ and ZZ production in the POWHEG BOX", *JHEP* **11** (2011) 078, doi:10.1007/JHEP11(2011)078, arXiv:1107.5051.

[25] P. Nason and G. Zanderighi, "W^+W^- , WZ and ZZ production in the POWHEG BOX V2", *Eur. Phys. J. C* **74** (2014) 2702, doi:10.1140/epjc/s10052-013-2702-5, arXiv:1311.1365.

[26] LHC Higgs Cross Section Working Group Collaboration, "Handbook of LHC Higgs cross sections: 4. Deciphering the nature of the Higgs sector", doi:10.23731/CYRM-2017-002, arXiv:1610.07922.

[27] NNPDF Collaboration, "Parton distributions for the LHC Run II", *JHEP* **04** (2015) 040, doi:10.1007/JHEP04(2015)040, arXiv:1410.8849.

[28] T. Sjöstrand, S. Mrenna, and P. Z. Skands, "A brief introduction to PYTHIA 8.1", *Comput. Phys. Commun.* **178** (2008) 852, doi:10.1016/j.cpc.2008.01.036, arXiv:0710.3820.

[29] J. Alwall et al., "Comparative study of various algorithms for the merging of parton showers and matrix elements in hadronic collisions", *Eur. Phys. J. C* **53** (2008) 473, doi:10.1140/epjc/s10052-007-0490-5, arXiv:0706.2569.

[30] R. Frederix and S. Frixione, "Merging meets matching in MC@NLO", *JHEP* **12** (2012) 061, doi:10.1007/JHEP12(2012)061, arXiv:1209.6215.

[31] GEANT4 Collaboration, "GEANT4 — a simulation toolkit", *Nucl. Instrum. Meth. A* **506** (2003) 250, doi:10.1016/S0168-9002(03)01368-8.

[32] CMS Collaboration, "Measurements of $t\bar{t}$ cross sections in association with b jets and inclusive jets and their ratio using dilepton final states in pp collisions at $\sqrt{s} = 13$ TeV", (2017). arXiv:1705.10141. Submitted to *Phys. Lett. B*.

[33] CMS Collaboration, "The CMS experiment at the CERN LHC", *JINST* **3** (2008) S08004, doi:10.1088/1748-0221/3/08/S08004.

[34] CMS Collaboration, "The CMS trigger system", *JINST* **12** (2017) P01020, doi:10.1088/1748-0221/12/01/P01020, arXiv:1609.02366.

[35] CMS Collaboration, "Particle-flow reconstruction and global event description with the CMS detector", (2017). arXiv:1706.04965. Submitted to *JINST*.

[36] CMS Collaboration, "Performance of electron reconstruction and selection with the CMS detector in proton-proton collisions at $\sqrt{s} = 8$ TeV", *JINST* **10** (2015) P06005, doi:10.1088/1748-0221/10/06/P06005, arXiv:1502.02701.

[37] CMS Collaboration, "Performance of CMS muon reconstruction in pp collision events at $\sqrt{s} = 7$ TeV", *JINST* **7** (2012) P10002, doi:10.1088/1748-0221/7/10/P10002, arXiv:1206.4071.

[38] M. Cacciari, G. P. Salam, and G. Soyez, "The anti-k_t jet clustering algorithm", *JHEP* **04** (2008) 063, doi:10.1088/1126-6708/2008/04/063, arXiv:0802.1189.

[39] M. Cacciari, G. P. Salam, and G. Soyez, "FastJet user manual", *Eur. Phys. J. C* **72** (2012) 1896, doi:10.1140/epjc/s10052-012-1896-2, arXiv:1111.6097.

[40] CMS Collaboration, "Determination of jet energy calibration and transverse momentum resolution in CMS", *JINST* **6** (2011) P11002, doi:10.1088/1748-0221/6/11/P11002, arXiv:1107.4277.

[41] CMS Collaboration, "Jet energy scale and resolution in the CMS experiment in pp collisions at 8 TeV", *JINST* **12** (2016) P02014, doi:10.1088/1748-0221/12/02/P02014, arXiv:1607.03663.

[42] CMS Collaboration, "Heavy flavor identification at CMS with deep neural networks", CMS Detector Performance Summary CMS-DP-2017-005, 2017.

[43] CMS Collaboration, "Performance of missing energy reconstruction in 13 TeV pp collision data using the CMS detector", CMS Physics Analysis Summary CMS-PAS-JME-16-001, 2016.

[44] CMS Collaboration, "Search for new physics in same-sign dilepton events in proton-proton collisions at $\sqrt{s} = 13\,\text{TeV}$", *Eur. Phys. J. C* **76** (2016) 439, doi:10.1140/epjc/s10052-016-4261-z, arXiv:1605.03171.

[45] CMS Collaboration, "CMS luminosity measurements for the 2016 data taking period", CMS Physics Analysis Summary CMS-PAS-LUM-17-001, 2017.

[46] CMS Collaboration, "Identification of b quark jets at the CMS experiment in the LHC Run2", CMS Physics Analysis Summary CMS-PAS-BTV-15-001, 2016.

[47] CMS Collaboration, "Search for Higgs boson production in association with top quarks in multilepton final states at $\sqrt{s}$ = 13 TeV", CMS Physics Analysis Summary CMS-PAS-HIG-17-004, 2017.

[48] ATLAS and CMS Collaborations, "Procedure for the lhc higgs boson search combination in summer 2011", ATL-PHYS-PUB-2011-011, CMS NOTE-2011/005, 2011.

[49] G. Cowan, K. Cranmer, E. Gross, and O. Vitells, "Asymptotic formulae for likelihood-based tests of new physics", *Eur. Phys. J. C* **71** (2011) 1554, doi:10.1140/epjc/s10052-011-1554-0, arXiv:1007.1727. [Erratum: *Eur. Phys. J. C* **73** (2013) 2501].

[50] T. Junk, "Confidence level computation for combining searches with small statistics", *Nucl. Instrum. Meth. A* **434** (1999) 435, doi:10.1016/S0168-9002(99)00498-2, arXiv:hep-ex/9902006.

[51] A. L. Read, "Presentation of search results: the CL_S technique", *J. Phys. G* **28** (2002) 2693, doi:10.1088/0954-3899/28/10/313.

[52] ATLAS and CMS Collaborations, "Measurements of the Higgs boson production and decay rates and constraints on its couplings from a combined ATLAS and CMS analysis of the LHC pp collision data at $\sqrt{s} = 7$ and 8 TeV", *JHEP* **08** (2016) 045, doi:10.1007/JHEP08(2016)045, arXiv:1606.02266.